MAGNETIC FIELD STRUCTURES AND PLASMA PROPERTIES OF HIGH-IOTA HIGH-MIRROR W7-X CONFIGURATIONS

E. Strumberger, R. Zille

IPP 2/333 **July 1996**

MAX-PLANCK-INSTITUT FÜR PLASMAPHYSIK

D-85748 Garching bei München, Germany

Die nachstehende Arbeit wurde im Rahmen des Vertrages zwischen dem Max-Planck-Institut für Plasmaphysik und der Europäischen Atomgemeinschaft über die Zusammenarbeit auf dem Gebiet der Plasmaphysik durchgeführt

Table of contents

Abstract

The coil system HS5V10T of Wendelstein 7-X is investigated with respect to its suitability for the attainment of stable, high-ι, high-mirror, low-shear, high-β plasma equilibria. For this purpose the coil currents of the modular coils and the auxiliary coils are varied individually, and a suitable current configuration is iteratively determined with the help of a system of numerical codes that allows to calculate vacuum magnetic fields and to trace field lines (GOURDON code), to determine fixed-boundary (VMEC code) and free-boundary equilibria (NEMEC code), to compute the magnetic fields of finite-β equilibria (MFBE code), to analyse the magnetic field properties (JMC code) and to determine the neoclassical properties (GUIDING CENTRE codes).

1.0 Introduction

Wendelstein 7-X (W7-X) [1, 2] is an optimized Helias-type (**HELI**cal **A**dvanced **S**tellarator) stellarator with $N = 5$ periods. For its optimization the following set of seven criteria has been used [3]:

- MHD properties

1. high quality of the (vacuum) magnetic surfaces,
2. good finite-β equilibrium properties,
3. good MHD stability properties,

- Neoclassical properties

4. small neoclassical transport in the lmfp regime,
5. small bootstrap current in the lmfp regime,
6. good collisionless α-particle confinement,

- Realization by coils

7. good modular coil feasibility.

The plasma behaviour in the confinement region is completely determined by the geometry of the confinement boundary within the last closed flux surface since this boundary yields a Neumann problem for the magnetic field inside of this boundary. Thus, the optimization with respect to the seven criteria given above was done by solving boundary value problems with the parameters of the plasma boundary being the optimization variables [4, 5].

After the plasma equilibrium had been specified, the modular coil system was determined. For this purpose the NESCOIL code (**NE**umann **S**olver for fields produced by external **COIL**s) [6] was developed to solve a Neumann problem at the plasma boundary in which a surface current was determined on an outer surface enclosing the plasma boundary, such that the normal component of the magnetic field produced by it was minimized at the plasma boundary. The resulting surface current distribution on this outer current-carrying surface was discretized into a finite number of current lines which represent the central current filaments of the actual finite-size coils. The shape of the outer surface and the number of Fourier components of the potential Φ, from which the current line had been calculated, were optimized with respect to technical aspects and the quality of the resulting magnetic field in comparison to the originally given field. As a result of these calculations a modular coil system called HS5V10N [7, 8] with 10 coils per field period has been obtained, which provides a magnetic field with nested magnetic surfaces and a specific rotational transform profile.

A flexible experimental device, however, requires a sufficently broad range of magnetic field parameters like the rotational transform, the magnetic well etc. This is achieved by a set of four planar coils per field period [7, 8], which is added to the coil set HS5V10N in a helical arrangement. The coil currents in the modular coils and these auxiliary coils are individually adjustable in order to produce various magnetic field configurations.

Investigations of various magnetic field configurations [7 – 10] produced with the coil set HS5V10N revealed an unfavourable aspect ratio for the high-ι case. Its plasma radius is nearly 20% smaller than that of the standard case. In order to improve the aspect ratio at high rotational transform values it was necessary to slightly modify the modular coils. It was possible to do this without significant changes of other magnetic parameters, e.g. the plasma radius and the rotational transform of the standard case, the shear, the magnetic well and the low harmonic Fourier components of the magnetic field [9] (see also sec. 3.1).

It has been the aim of this work to investigate this modified coil set called HS5V10T with respect to its suitability for the attainment of a stable, high-ι, high-mirror, low-shear, high-β plasma equilibrium. For this purpose, the currents of the modular and auxiliary coils are changed individually, and a suitable current configuration is determined iteratively using a system of numerical codes that allows to calculate vacuum magnetic fields and to trace field lines (GOURDON code), to determine fixed-boundary (VMEC code) [11, 12] and free-boundary equilibria (NEMEC code) [12], to compute the magnetic fields of finite-β equilibria (MFBE code) [13], to analyse the magnetic field properties (JMC code) [4, 14, 15] and to determine the neoclassical properties (GUIDING CENTRE codes), viz. the neoclassical transport [16, 17], the bootstrap current [18, 19] and the collisionless α-particle confinement [20].

This paper is organized as follows. Section 2 gives a description of the iteration procedure and the code system. Various vacuum magnetic fields, which are created by different current configurations, and their properties (e.g. ι-profile, magnetic well, magnetic mirror) are discussed in section 3. Finite-β equilibria, their magnetic field structures and their MHD stability properties are studied in section 4, while section 5 deals with the neoclassical transport and the bootstrap current in the lmfp regime and the collisionless α-particle confinement. A summary of the results and an outlook to further calculations are given in section 6 and, finally, a complete list of the numerical parameters used in the codes mentioned above is put together in the appendix.

2.0 Iteration procedure and code system

The coil system HS5V10T proposed for W7-X (major radius: $R_0 = 5.5$ m, plasma radius: $a_0 = 0.55$ m) consists of fifty modular non-planar coils and twenty auxiliary planar, non-circular coils, that is, ten modular and four auxiliary coils for each of the five periods. The coils are superconducting and produce a magnetic field strength of 3 T on the magnetic axis.

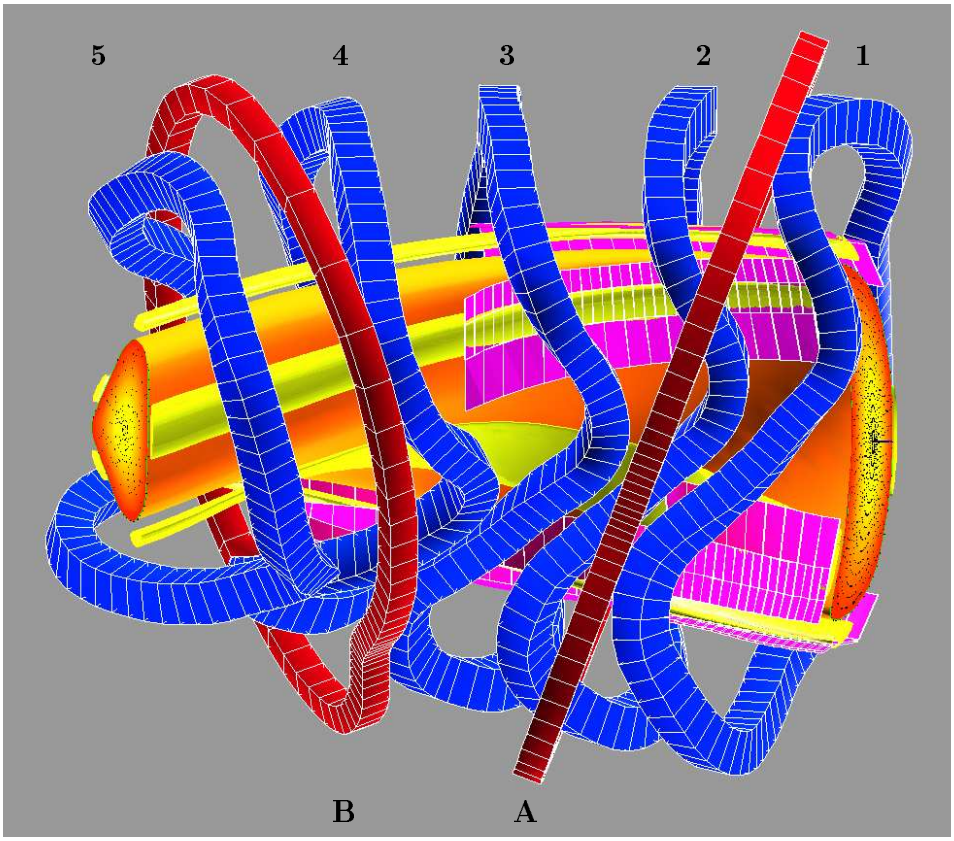

FIG. 1: Three-dimensional representation of the plasma tube (orange) of the so-called standard case (see section 2) and the coil set HS5V10T (blue: modular coils 1-5, reddish brown: auxiliary coils A and B) for half a period. The triangular cross-section on the left side and the bean-shaped cross-section on the right side include Poincaré plots of closed magnetic surfaces. Furthermore, the five islands of the standard case (yellow) and the proposed divertor and baffle plates (pink) [8, 21, 22], which are intersected by these islands, are shown.

Because of the periodicity and the stellarator symmetry only the five modular and the two auxiliary coil currents of half a period are free for variations, while the other currents are then determined by the symmetry conditions. That is, there are seven degrees of freedom to produce various magnetic fields.

An overview over the iteration procedure and the code system for optimizing the coil currents is given in Fig. 2. There the iteration loops are shown including the names of the corresponding numerical codes, which are used for the calculations. The iteration loops and the numerical codes are explained in the following.

- The seven coil currents form the **INPUT** of the iteration process.
- The coil currents are used to determine the vacuum magnetic field by means of Biot-Savart's law and to trace field lines using the **GOURDON** code. In addition to Poincaré plots of the magnetic field structure the GOURDON code yields the rotational transform and the magnetic well of the vacuum magnetic field. Furthermore, the last closed magnetic surface (lcms) is determined.
- The data of the coordinates along the field line forming the lcms are used in the **DESCUR** code [23] to approximate the lcms by a set of Fourier coefficients. These Fourier coefficients are the input of the fixed boundary equilibrium VMEC code and the free-boundary equilibrium NEMEC code.
- The **VMEC** code (**V**ariational **M**oments **E**quilibrum **C**ode) [11, 12] (here only used in the vacuum case) is an energy minimizing fixed boundary equilibrium code assuming nested flux surfaces. It determines the plasma equilibrium inside a given fixed boundary (which is the lcms in the vacuum case) and yields the Fourier coefficients of the nested flux surfaces and of the magnetic field on these surfaces as well as the rotational transform and the magnetic well.
- The 3D free-boundary equilibrium **NEMEC** code [12] is a synthesis of the VMEC code and the NESTOR (**NE**umann **S**olver for **TO**roidal **R**egions) vacuum code [24]. It is used to determine free-boundary finite-β Helias equilibria. It yields the Fourier coefficients of the nested flux surfaces inside and on the plasma boundary, the Fourier coefficients of the magnetic field on these flux surfaces and the Fourier coefficients of the potential Φ on the plasma boundary, which determines the magnetic field outside the plasma boundary. Furthermore, it calculates the rotational transform on the flux surfaces, the magnetic well and the plasma volume of the finite-β equilibrium.
- In order to compute the magnetic fields of finite-β equilibria on a grid inside and outside the plasma boundary the **MFBE** code (**M**agnetic Field Solver for **F**inite-**B**eta **E**quilibria) [13] is used. This magnetic field defined on a grid serves as input to the GOURDON code, which traces field lines inside and outside the plasma boundary and determines the lcms of the finite-β equilibrium. If this lcms does not coincide with the plasma boundary obtained by the NEMEC code, the toroidal flux, which is a free parameter in the NEMEC code, is modified, that is, the toroidal flux is determined iteratively (see [13]).

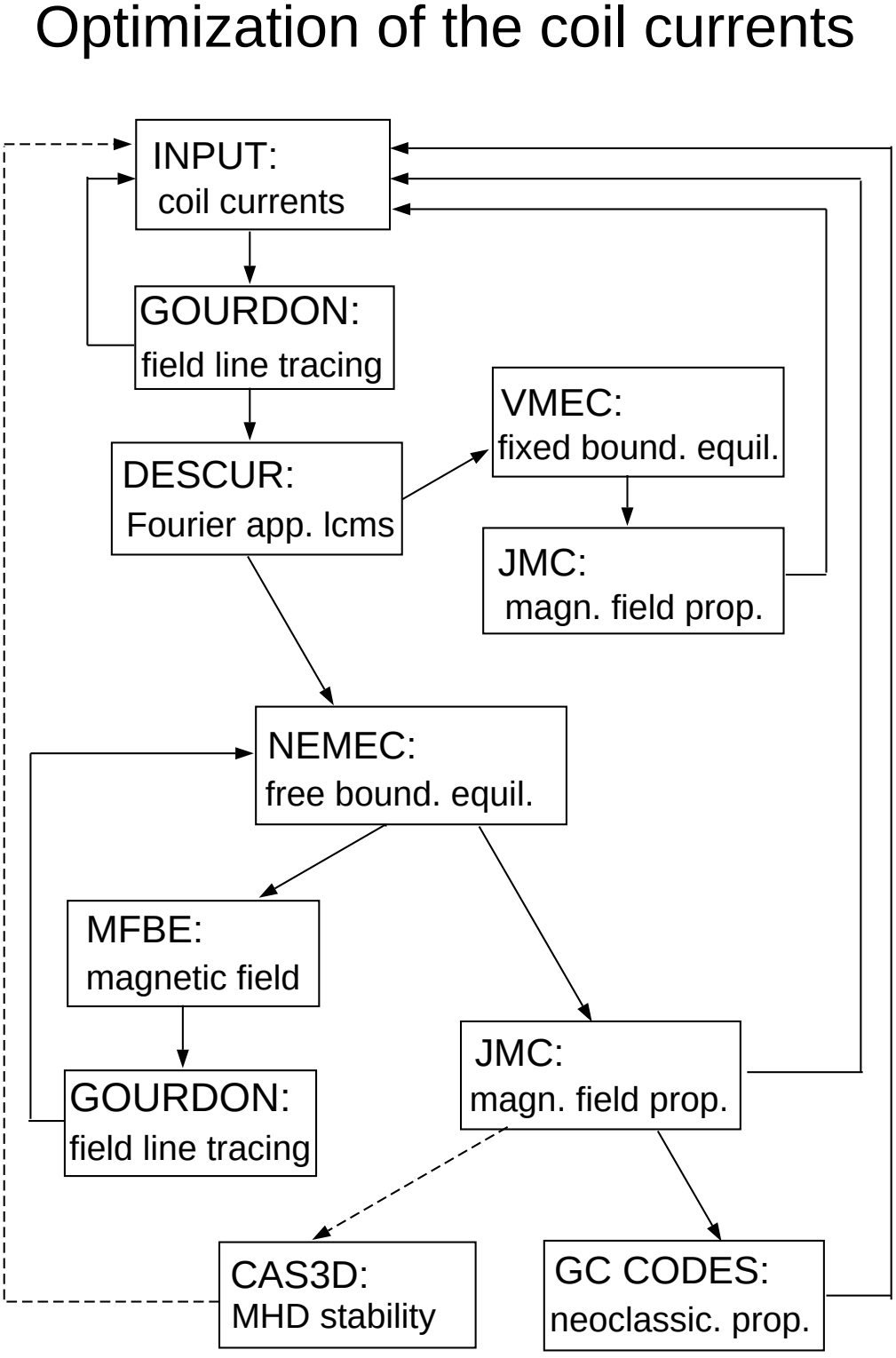

FIG. 2: Overview of the iteration procedure and the code system for optimizing the coil currents.

- The natural coordinates for calculating local and global instabilities and neoclassical properties are the magnetic coordinates [25]. Therefore, the **JMC** code transforms the curvilinear coordinates (s, u, v) [11] used in the VMEC and the NEMEC code into the magnetic coordinates and yields the Fourier spectrum of the magnetic field, which determines the neoclassical properties. Furthermore, the stability of the three-dimensional finite-β equilibria with respect to Mercier [26] and resistive interchange modes [27] is studied by means of the JMC code [4, 5, 15]. If the Fourier spectrum of the magnetic field shows undesirable properties or if the stability criteria of Mercier and resistive interchange modes are not fulfilled the coil currents are modified and the calculations start from the beginning.
- The neoclassical transport [16, 17], the bootstrap current [18, 19] and the collisionless α-particle confinement [20] are calculated with various GUIDING CENTRE codes (**GC** codes). In the case of unfavourable neoclassical properties the coil currents are modified.
- The **CAS3D** code [28] is a stability code for nonlocal mode analysis starting from the formulation of the MHD energy functional in magnetic coordinates. It has been shown that in Helias stellarators Mercier mode stability has to be satisfied to avoid global modes and low poloidal number ballooning modes then do not exist [3]. The CAS3D code has therefore not been used within the iteration procedure described here.

3. Properties of the vacuum magnetic fields

3.1 Comparison of HS5V10N and HS5V10T

First, the magnetic fields produced with the coil sets HS5V10N and HS5V10T will be compared in this section.

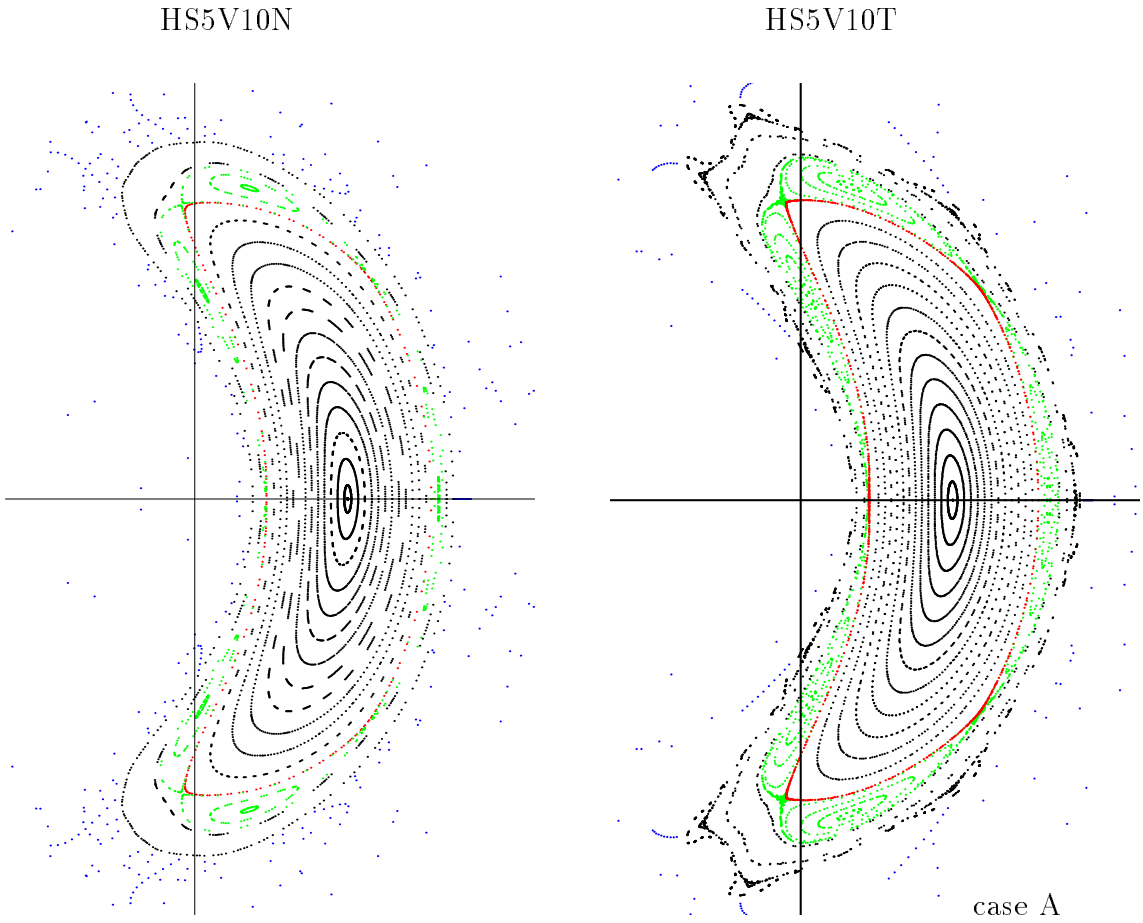

FIG. 3a: Poincaré plots of the vacuum magnetic fields of the standard cases (case A) for HS5V10N and HS5V10T. At the symmetric bean-shaped cross-section flux surfaces (black dots), a chain of five islands (green dots), the last closed magnetic surface (red dots) and ergodic field lines (blue dots) are plotted.

Figures 3a,b show the vacuum magnetic field structures of the standard cases (case A) with five macroscopic islands and the high-ι cases (case B) with four macroscopic islands outside the last closed magnetic surface (for the corresponding coil currents see Tab. II in sec. 3.2). With respect to the proposed divertor concept [8, 21, 22] - the divertor plates intersect the macroscopic islands [10] - the lcms is defined as the last closed magnetic surface inside the macroscopic islands (red dots in Figs 3a,b). In case A

only small changes in the magnetic field structure prevail (compare also Tab. I), while important differences occur in case B. There, using the coil set HS5V10T, the volume inside the lcms increases, i.e. the aspect ratio decreases (see Tab. I) and the ergodization of the edge region is reduced, i.e. the remnants of the macroscopic islands are enlarged.

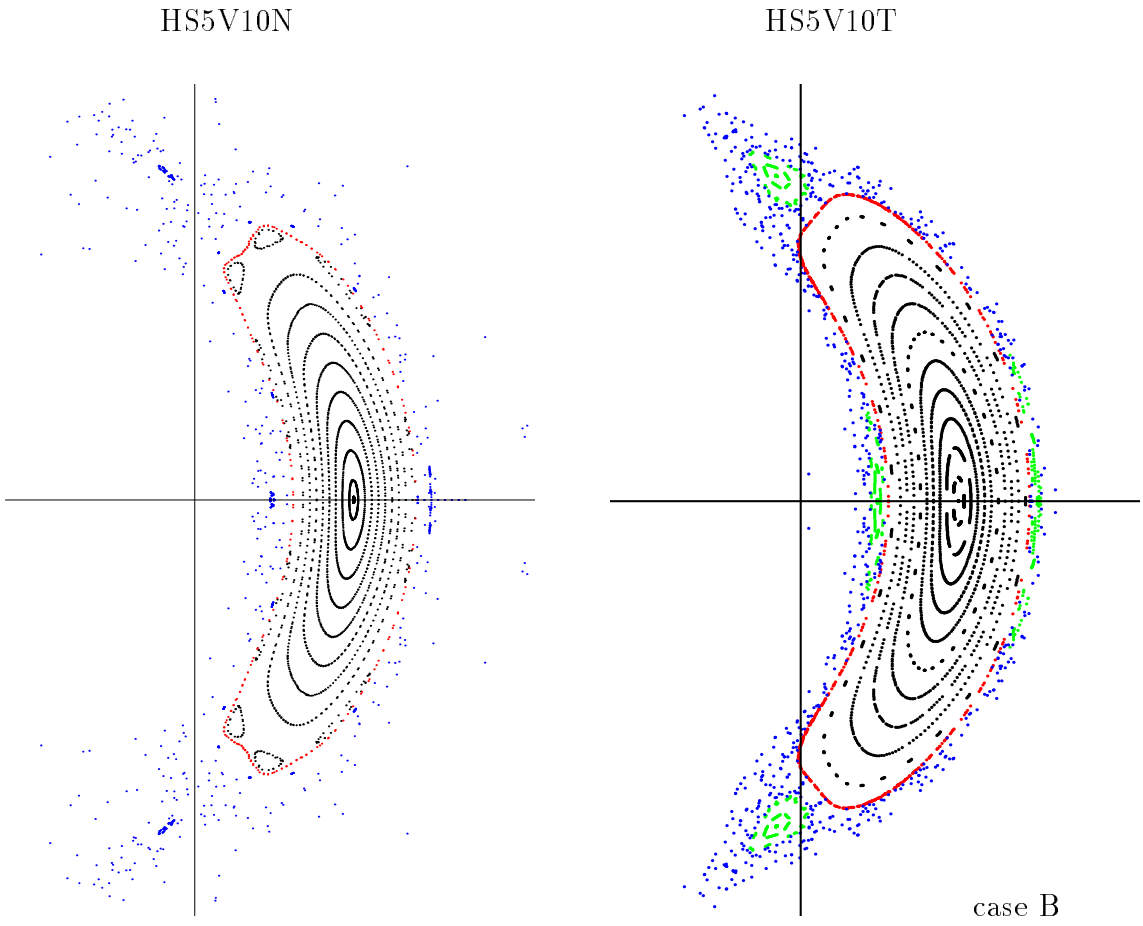

FIG. 3b: Poincaré plots of the vacuum magnetic fields of the high-ι cases (case B) for HS5V10N and HS5V10T. At the symmetric bean-shaped cross-section flux surfaces (black dots), four islands (green dots), the last closed magnetic surface (red dots) and ergodic field lines (blue dots) are plotted.

The Fourier representation of the magnetic field B in magnetic coordinates [14, 25] is given by

$$B = \sum_{\mathrm{m,n}} B_{\mathrm{m,n}}(s)\cos[2\pi(\mathrm{m}\theta - \mathrm{n}\phi)],$$

with s the flux label and θ, ϕ the poloidal (index m) and toroidal (index n) variables. A complete Fourier description of the W7-X magnetic field produced by a set of modular and auxiliary coils needs a rather large number of contributing harmonics, the great majority of which may be assigned to one of three groups according to their toroidal

mode number n. These groups are identified with (1) the toroidal nature of the device (n=0); (2) the stellarator structure (typically $1 \leq \mathrm{n} \leq 3$); and (3) the modular ripple (typically $8 \leq \mathrm{n} \leq 12$). In particular, the component $B_{0,0}$ describes the main magnetic field containing the deepening of the magnetic well at finite β, $B_{1,1}$ represents the helical curvature, $B_{1,0}$ the toroidal curvature and $B_{0,1}$ the mirror field.

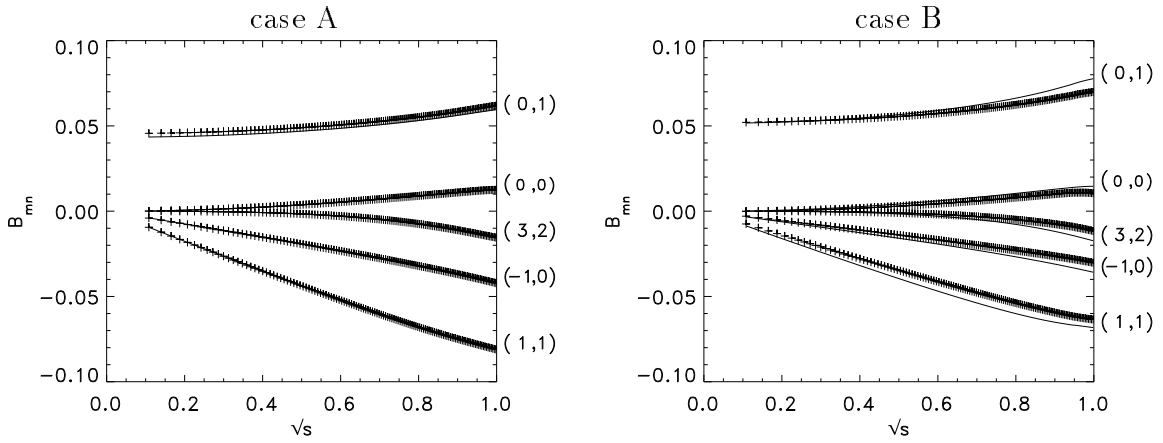

FIG. 4: Comparison of the largest Fourier coefficients $B_{\mathrm{m,n}}$ of HS5V10N (+) and HS5V10T (solid line) for the cases A and B. The $B_{\mathrm{m,n}}$s are plotted versus $\sqrt{s}$. Fourier coefficients smaller than 0.01 are not shown. $B_{0,0}(s = 0) = 1$ has been subtracted in plotting $B_{0,0}$.

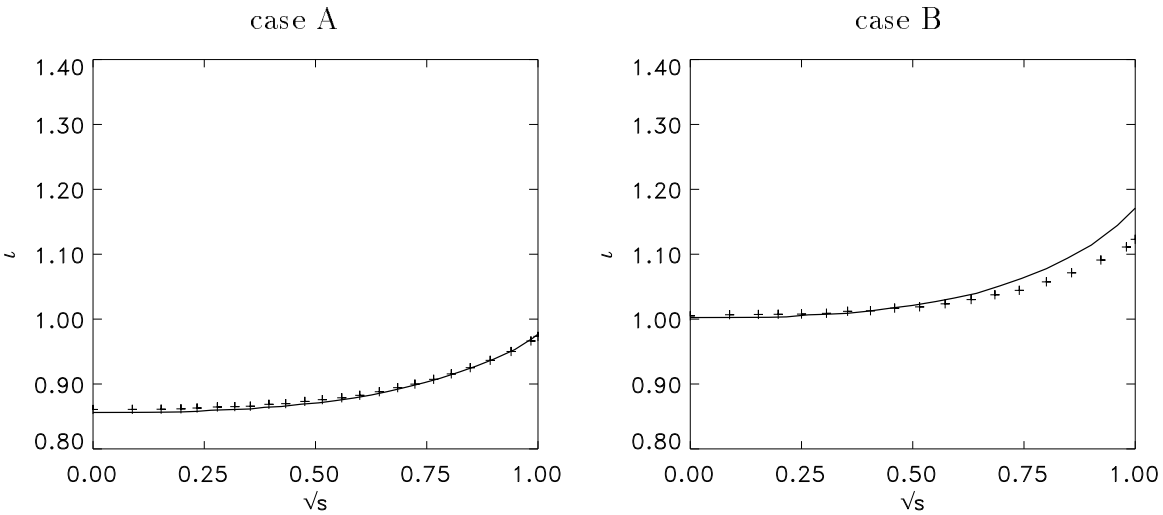

FIG. 5: Comparison of the rotational transforms ι of HS5V10N (+) and HS5V10T (solid line) for the cases A and B.

In Fig. 4 only the largest Fourier coefficients $B_{\mathrm{m,n}}$ of cases A and B versus $\sqrt{s}$ are shown. For clarity, Fourier coefficients smaller than 0.01 are neglected. $B_{0,0}(s = 0) = 1$

is subtracted in plotting $B_{0,0}$. For the standard case (case A) the $B_{\mathrm{m,n}}$s of the old coil set HS5V10N denoted with + and the coefficients of the new coil set HS5V10T represented by solid lines are almost the same, while in the high-ι case (case B) small deviations occur. The Fourier coefficient $B_{0,1}$ corresponds to a mirror field of approximately 5% for the standard case and is slightly increased ($\approx 6\%$) for the high-ι case.

The profiles of the rotational transform ι and the magnetic well V'' are plotted for the cases A and B in Figs 5 and 6 comparing the two coil sets. Again no deviations are visible in the standard case, while for the high-ι case a small deepening occurs.

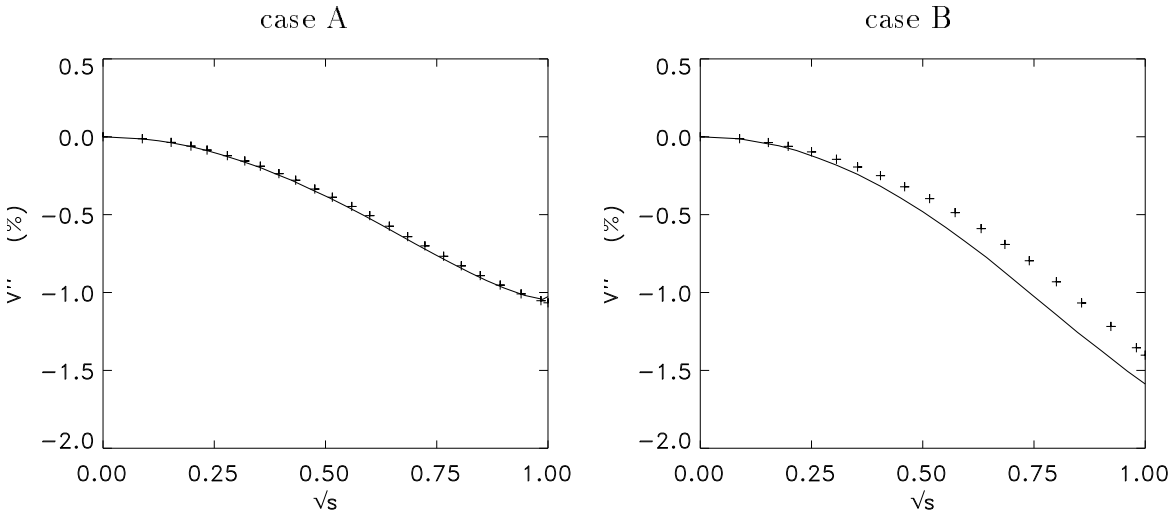

FIG. 6: Comparison of the magnetic wells V'' of HS5V10N (+) and HS5V10T (solid line) for the cases A and B.

TABLE I: Rotational transform ι_0 on the magnetic axis, aspect ratio A, magnetic well $V'' = (V'_{lcms} - V'_0)/V'_0$ (V'_{lcms} = specific volume on the lcms, V'_0 = specific volume on the magnetic axis) and volume V enclosed by the lcms for the vacuum magnetic field configurations A and B produced by the coil sets HS5V10N and HS5V10T.

case A

coil set	ι_0	A	V'' [%]	V [m^3]
HS5V10N	0.861	10.69	-1.07	28.88
HS5V10T	0.856	10.79	-1.03	28.48

case B

coil set	ι_0	A	V'' [%]	V [m^3]
HS5V10N	1.005	12.91	-1.40	19.99
HS5V10T	1.002	11.24	-1.59	25.96

The results of the comparisons are summed up in Table I, which contains the rotational transform ι_0 on the magnetic axis, the aspect ratio A, the magnetic well V'' and the volume V inside the lcms of cases A and B for the two coil sets. While the magnetic field properties of the standard case are almost unchanged, the high-ι case is improved by the new coil set HS5V10T, that is, the aspect ratio is reduced so that the volume inside the lcms increases substantially.

The comparisons of the standard cases and the high-ι cases show that an increase of the rotational transform leads to an increase of the aspect ratio and a reduction of the volume inside the lcms. The rotational transform of the high-ι case is only slightly higher than unity on the magnetic axis. That is, for the corresponding finite-β equilibrium with high average β the rotational transform will fall below unity - an increase of β leads to a decrease of the rotational transform - so that the low-order rational value (5/5) occurs inside the plasma. In the next section the coil currents are varied in order to find a vacuum magnetic field configuration with a higher ι-value at the magnetic axis without a too large reduction of the volume inside the lcms.

3.2 High-ι, high-mirror magnetic fields

To produce a high-ι, high-mirror vacuum magnetic field with reduced shear the coil currents have to be chosen suitably. Table II contains the currents of the modular coils 1,...,5 and the planar coils A and B for five magnetic field configurations of W7-X.

TABLE II: Currents of the modular coils 1...5 and the planar coils A and B for five different magnetic field configurations of W7-X. $I_{\rm n}$ [MA] is the nominal coil current for producing a magnetic field strength of $\langle B_0 \rangle = 2.5$ T, which is averaged along the magnetic axis. $F_{\rm c}$ is the factor related to the cases A-E for each coil type given in the table leading to an individual coil current $I_{\rm c} = I_{\rm n} F_{\rm c}$.

	I_n	F_c						
case	[MA]	1	2	3	4	5	A	B
A	1.450	1.000	1.000	1.000	1.000	1.000	0.0	0.0
B	1.593	1.000	1.000	1.000	1.000	1.000	-0.220	-0.220
C	1.556	1.064	1.105	0.962	1.013	0.972	-0.235	-0.235
D	1.717	1.116	1.085	0.846	0.785	0.734	-0.300	-0.125
E	1.779	0.981	1.003	0.846	0.846	0.827	-0.315	-0.150

Case A, the so-called standard case, which has already been discussed in the previous section, is realized by equal modular coil currents and no planar coil currents. In order to obtain the high-ι case (case B, see previous section), equal currents through the planar coils are added. To realize a high mirror the modular coil currents have to be varied (case C, high-ι, high-mirror case), and for reducing the shear the currents of the planar coils have to be different (cases D and E, high-ι, high-mirror, low-shear cases).

Figure 7 shows the vacuum magnetic field structures of cases C, D and E for the bean-shaped cross-section and in Figs 8, 9 and 10 the corresponding Fourier coefficients of the magnetic field, the profiles of the rotational transform and the profiles of the magnetic well are plotted. While the rotational transform on the magnetic axis increases from case C to case E, the volume inside the lcms decreases (see Fig. 7 and compare also Tab. III). That is, a decrease of the shear, as it is realized in case D and case E (see Fig. 9), is accompanied by a volume loss. While the auxiliary coil currents influence mainly the profile of the rotational transform, the mirror is influenced by the modular coil currents. Case D therefore has the largest mirror field of the three cases (see Fig. 8). Its Fourier coefficient $B_{0,1}$ amounts to 20%, which is twice as large as in case C and case E. Furthermore, the magnetic well depth of case D is clearly reduced with respect to the cases C and E (see Fig. 10).

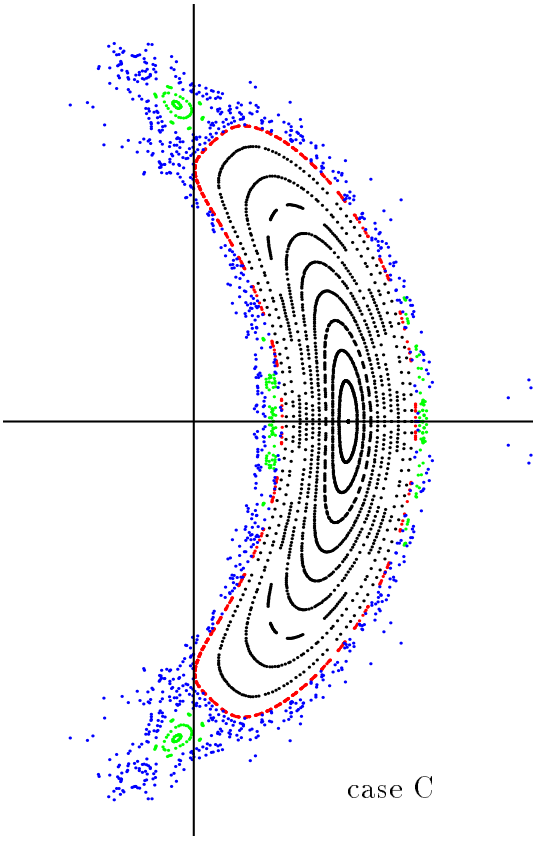

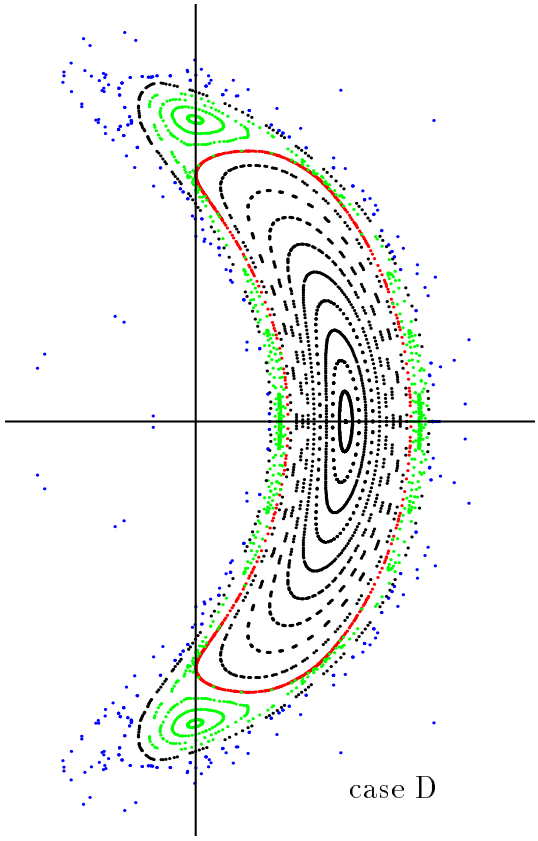

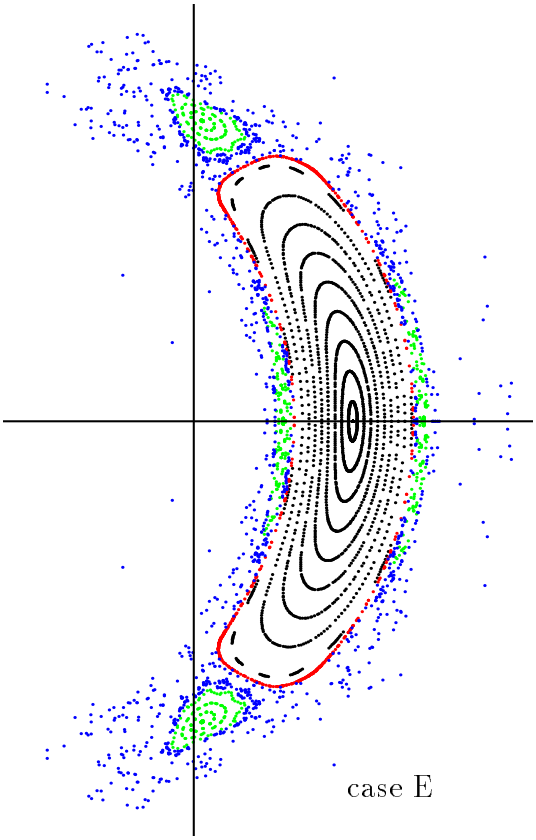

FIG. 7: Poincaré plots of the vacuum magnetic fields of cases C, D and E. At the symmetric bean-shaped cross-section flux surfaces (black dots), four islands (green dots), the last closed magnetic surface (red dots) and ergodic field lines (blue dots) are plotted.

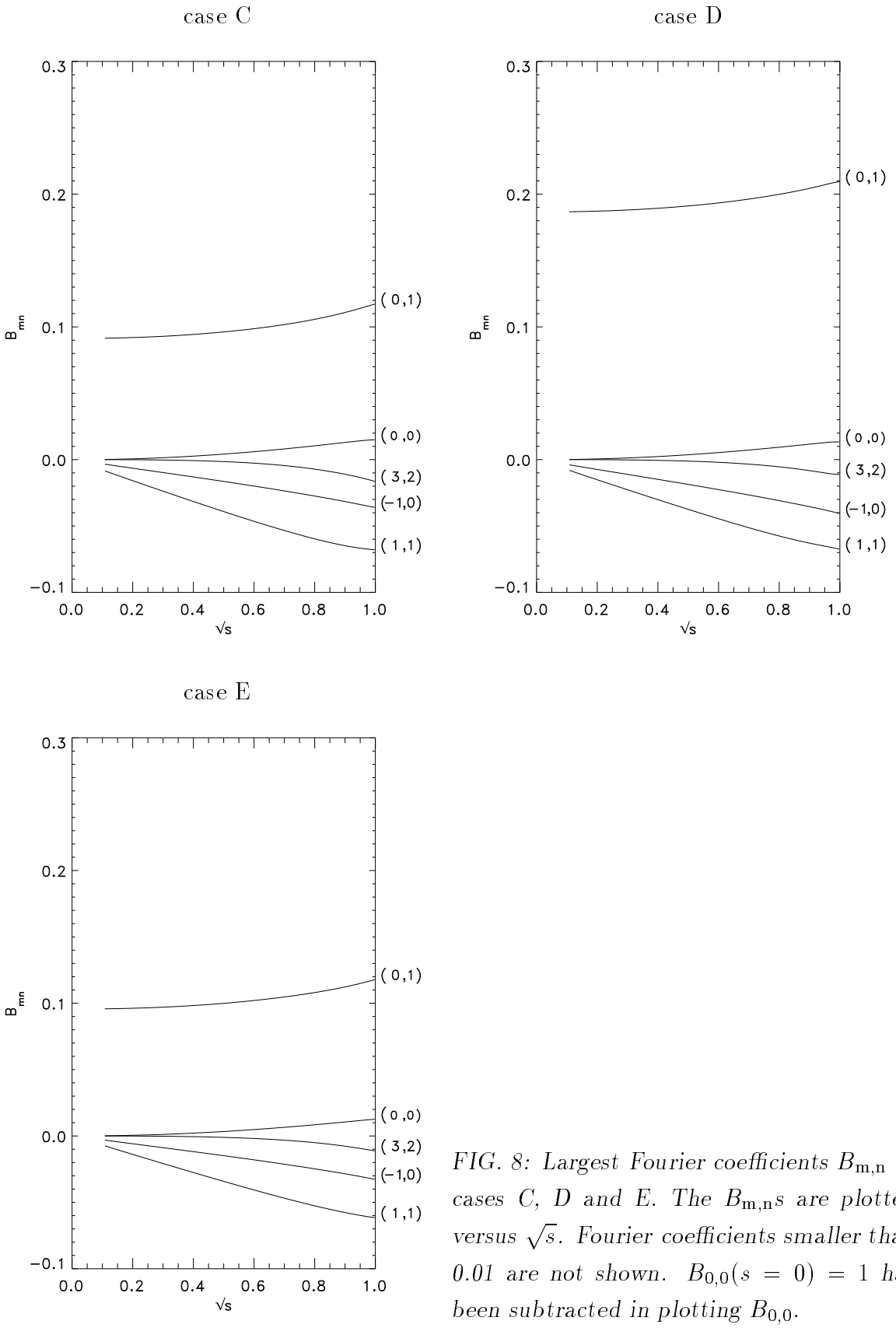

FIG. 8: Largest Fourier coefficients $B_{\mathrm{m,n}}$ of cases C, D and E. The $B_{\mathrm{m,n}}$s are plotted versus $\sqrt{s}$. Fourier coefficients smaller than 0.01 are not shown. $B_{0,0}(s = 0) = 1$ has been subtracted in plotting $B_{0,0}$.

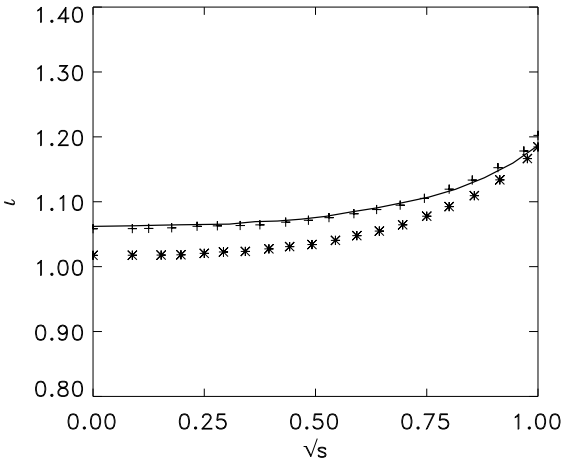

FIG. 9: Comparison of the rotational transforms ι of cases C (∗), D (+) and E (solid line).

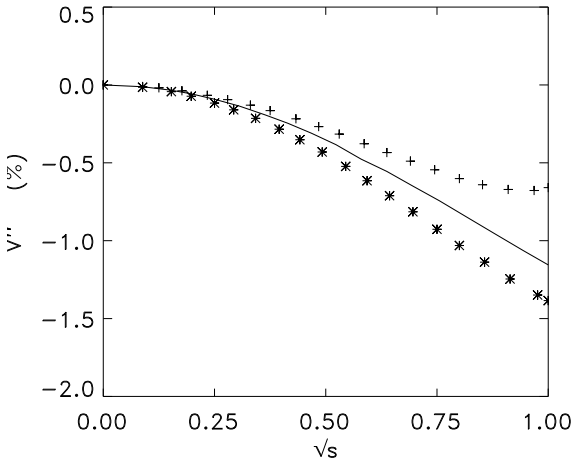

FIG. 10: Comparison of the magnetic wells V'' of cases C (∗), D (+) and E (solid line).

The results of the comparisons of cases C, D and E are summed up in Table III, which contains the rotational transform ι_0 on the magnetic axis, the aspect ratio A, the magnetic well V'' and die volume V inside the lcms.

TABLE III: Rotational transform ι_0 on the magnetic axis, aspect ratio A, magnetic well $V'' = (V'_{lcms} - V'_0)/V'_0$ (V'_{lcms} = specific volume on the lcms, V'_0 = specific volume on the magnetic axis) and volume V enclosed by the lcms for the vacuum magnetic field configurations C, D and E.

case	ι_0	A	V'' [%]	V [m^3]
C	1.018	11.41	-1.38	25.19
D	1.058	11.80	-0.66	24.38
E	1.062	12.85	-1.16	20.48

4. MHD properties

4.1 Finite-β magnetic field properties

The newly developed MFBE code [13] allows extended investigations of the finite-β structure of the magnetic field. It computes the finite-β magnetic field inside and outside the plasma boundary and, thus, makes an iterative determination of the lcms possible.

Free-boundary equilibria with an average beta of $\langle\beta\rangle = 0.04$ are computed by means of the NEMEC code for the high-ι, high-mirror cases C, D and E, and the corresponding magnetic fields of these equilibria are determined on a grid by using the MFBE code. Figure 11 shows the Poincaré plots of the magnetic fields of cases C, D and E for the bean-shaped cross-sections. They are the results of the iteration procedure that allows to find the lcms by coupling of the NEMEC and the MFBE code [13].

The comparison of the finite-β fields with the corresponding vacuum fields given in Fig. 7 shows that the volume inside the lcms decreases, i.e. the aspect ratio increases (see also Tables III and IV). Furthermore, the magnetic axis is slightly moved in outward direction and the ergodization of the edge region is increased. The large remnants of the 5/4-islands, which prevail in the edge regions of the vacuum fields of cases C and E, almost disappear for $\langle\beta\rangle = 0.04$, while the closed magnetic surfaces in the vacuum edge region of case D ergodize and relatively large remnants of the 5/4-islands are still found in the finite-β field.

In Fig. 12 the largest Fourier coefficients $B_{\mathrm{m,n}}$ of the magnetic fields of cases C, D and E are given for $\langle\beta\rangle = 0.04$. All Fourier components except $B_{0,0}$ depend only weakly on β (compare Fig. 8). This is a consequence of the weak change in geometry of the flux surfaces as β is increased (see Figs 7 and 11).

The pressure profiles and the rotational transform profiles of cases C, D and E with $\langle\beta\rangle = 0.04$ are plotted in Figs 13 and 14. The steepest pressure profile belongs to case E, while it flattens from case E to D because of the increasing plasma volume (see Tab. IV). The rotational transform $\iota_0(0)$ on the magnetic axis lies above unity for the cases D and E and below unity for case C. In the latter case this low rotational transform value appears at approximately half the plasma radius (see Figs 11 and 14).

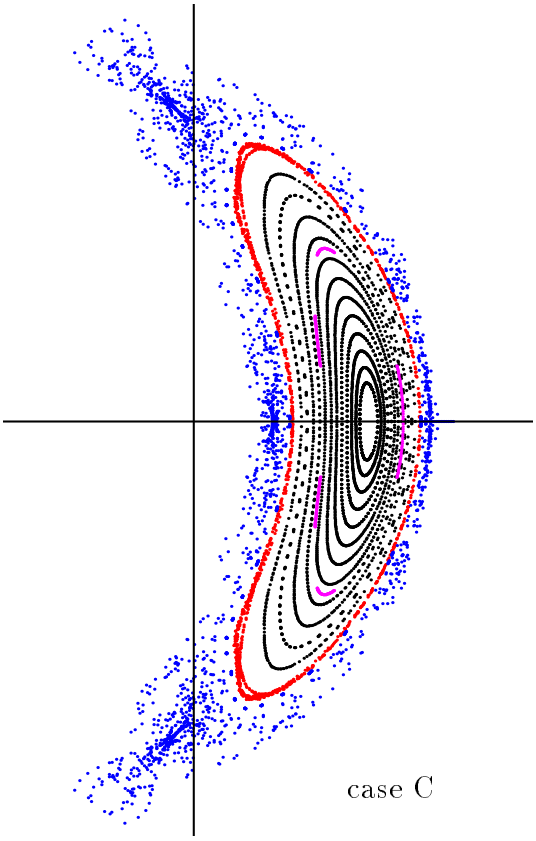

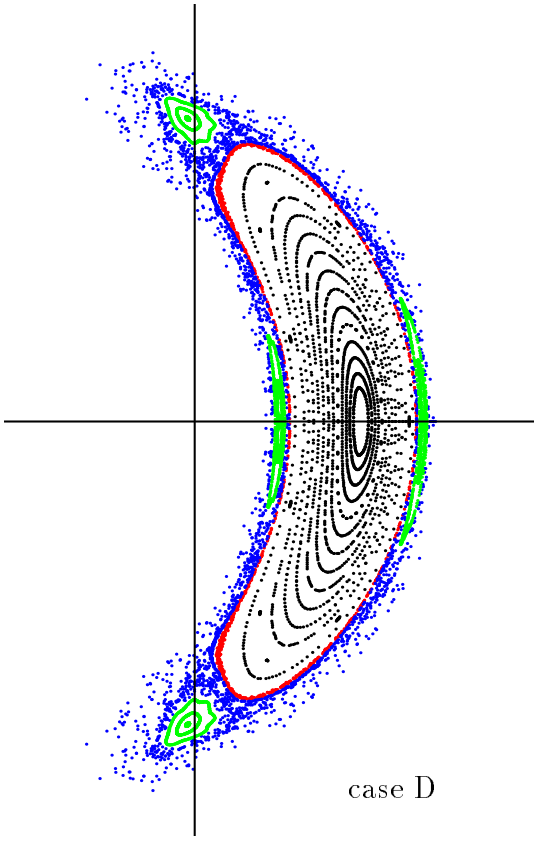

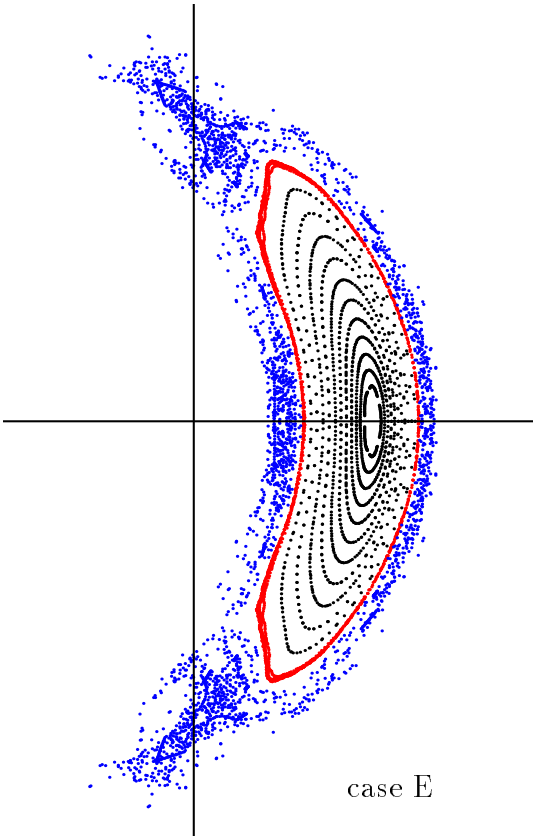

FIG. 11: Poincaré plots of the magnetic fields of cases C, D and E for $\langle\beta\rangle = 0.04$. *At the symmetric bean-shaped cross-section flux surfaces (black dots), four islands (green dots), the last closed magnetic surface (red dots) and ergodic field lines (blue dots) are plotted. In case C the rotational transform value* $\iota = 5/5$ *(pink dots) appears at approximately half the plasma radius.*

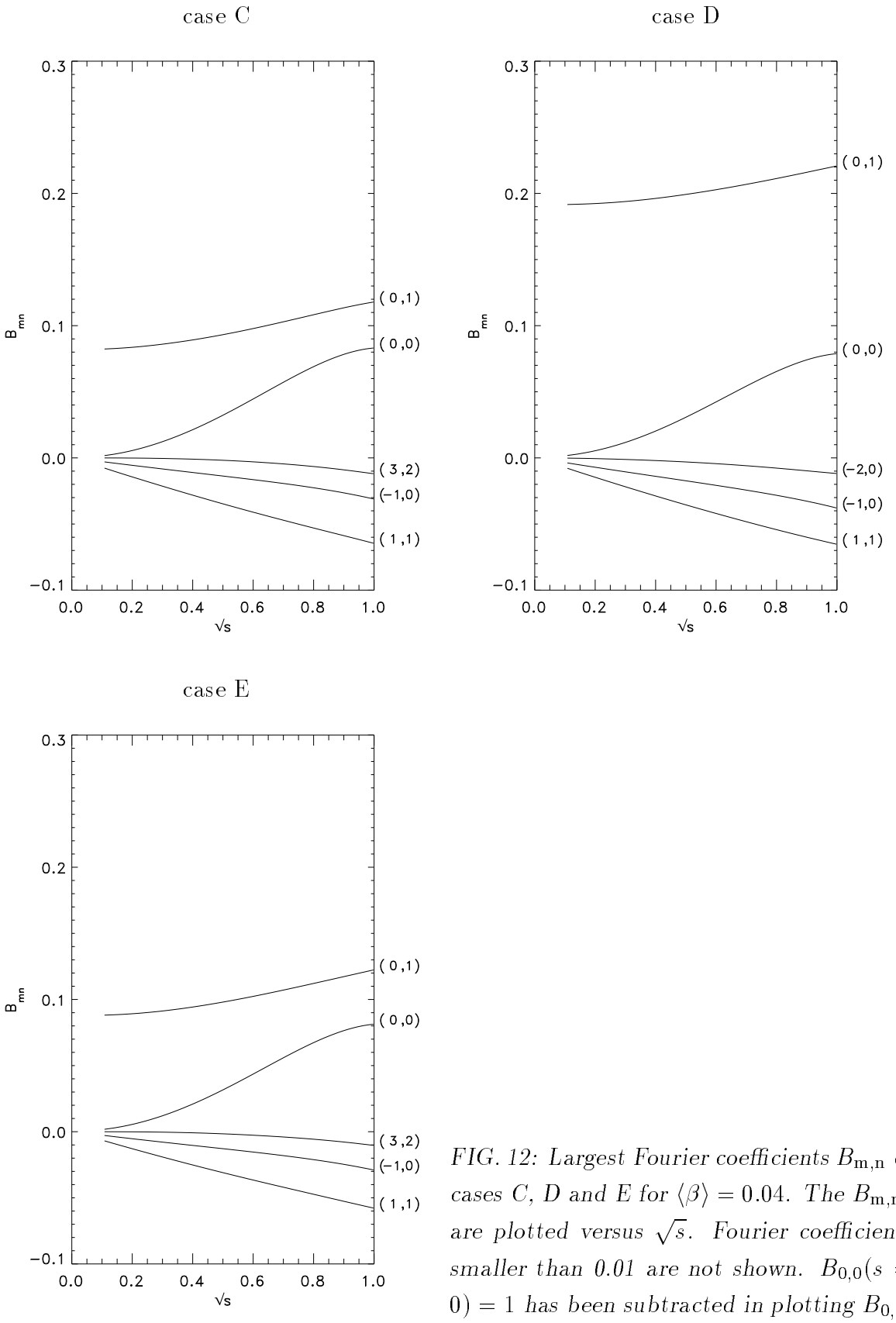

FIG. 12: Largest Fourier coefficients $B_{\mathrm{m,n}}$ of cases C, D and E for $\langle\beta\rangle = 0.04$. The $B_{\mathrm{m,n}}$s are plotted versus $\sqrt{s}$. Fourier coefficients smaller than 0.01 are not shown. $B_{0,0}(s = 0) = 1$ has been subtracted in plotting $B_{0,0}$.

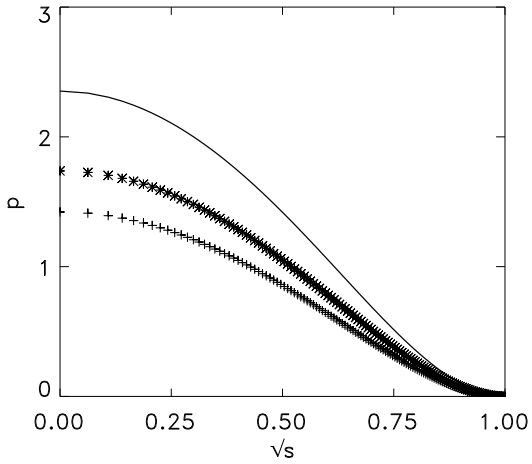

FIG. 13: Comparison of the pressure profiles p of cases C $(*)$, D $(+)$ and E (solid line) for $\langle\beta\rangle = 0.04$.

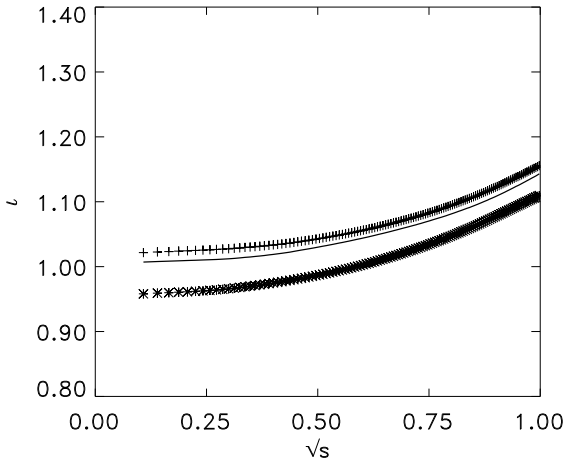

FIG. 14: Comparison of the rotational transforms ι of cases C $(*)$, D $(+)$ and E (solid line) for $\langle\beta\rangle = 0.04$.

The results of the comparisons of cases C, D and E for $\langle\beta\rangle = 0.04$ are summed up in Table IV, which contains the β-value β_0 on the magnetic axis, the rotational transform ι_0 on the magnetic axis, the aspect ratio A and the volume V inside the lcms.

TABLE IV: β-value β_0 on the magnetic axis, rotational transform ι_0 on the magnetic axis, aspect ratio A and volume V enclosed by the lcms for the magnetic field configurations C, D and E with $\langle\beta\rangle = 0.04$.

case	β_0	ι_0	A	V [m^3]
C	0.121	0.957	12.92	20.53
D	0.116	1.020	12.38	22.70
E	0.121	1.006	14.07	17.73

4.2 MHD stability properties

The MHD stability properties of finite-β equilibria ($\langle\beta\rangle = 0.04$) are studied with respect to the Mercier [26] and resistive interchange [27] criteria by means of the JMC code [4, 14, 15].

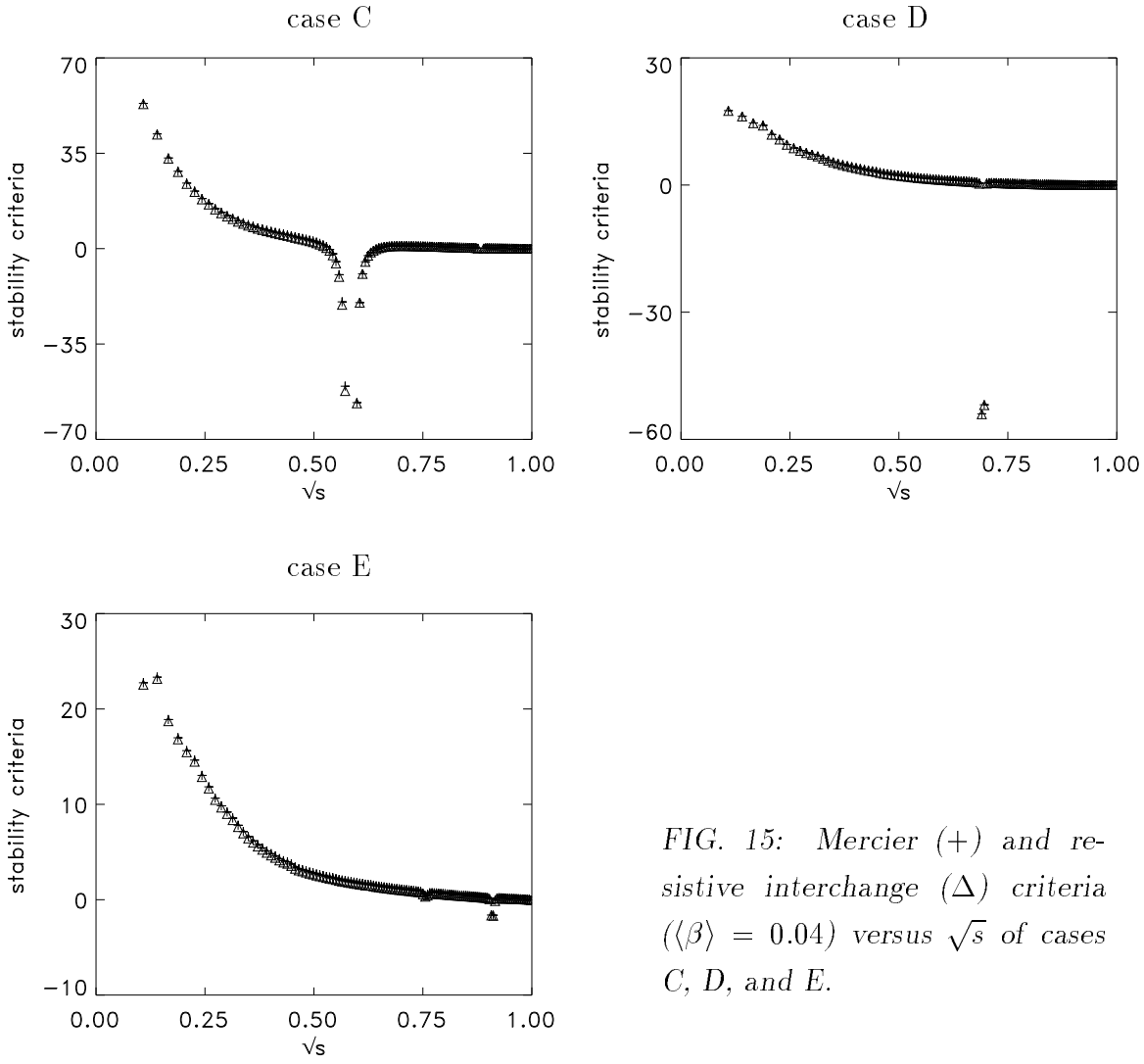

FIG. 15: Mercier (+) and resistive interchange (Δ) criteria ($\langle\beta\rangle = 0.04$) versus $\sqrt{s}$ of cases C, D, and E.

Figure 15 shows the Mercier (+) and resistive interchange (Δ) criteria of cases C, D, and E. While for case C a finite region of formal instability prevails around $\sqrt{s} = 0.6$ ($\iota(0.6) = 5/5$), cases D and E are stable. Therefore, only the cases D and E will be studied with respect to their neoclassical properties in the next section. In these latter two cases only higher rational values occur, viz. $\iota(0.69) = 15/14$ for case D, and $\iota(0.75) = 15/14$ and $\iota(0.91) = 10/9$ for case E. Since the free-boundary equilibrium computations were made with m=0,1,2,...,14, n=-12,...,0,...,12 Fourier coefficients, only the resonances m/n=5/5 of case C and m/n=10/9 of case E are at least formally resolved by these calculations (for details see appendix).

5. Neoclassical properties

5.1 Neoclassical transport

The structure of the magnetic field in terms of its Fourier components $B_{\mathrm{m,n}}$ as shown in Fig. 12 governs the neoclassical properties. In the long mean free path (lmfp) regime particles trapped in local 'ripple' wells created by these Fourier harmonics determine the neoclassical transport rate. For W7-X these local wells are of two types: the basic non-axisymmetric structure of B (typically $1 \leq \mathrm{n} \leq 3$) and the modular ripple (typically $8 \leq \mathrm{n} \leq 12$). The latter is a consequence of the discrete nature of the individual coils which produce the W7-X magnetic field. Figure 16 shows the modular ripple spectra of cases D and E for $\langle\beta\rangle = 0.04$. In both cases these components have been neglected in the following calculations (see appendix) because of their very small values ($< 0.4\%$).

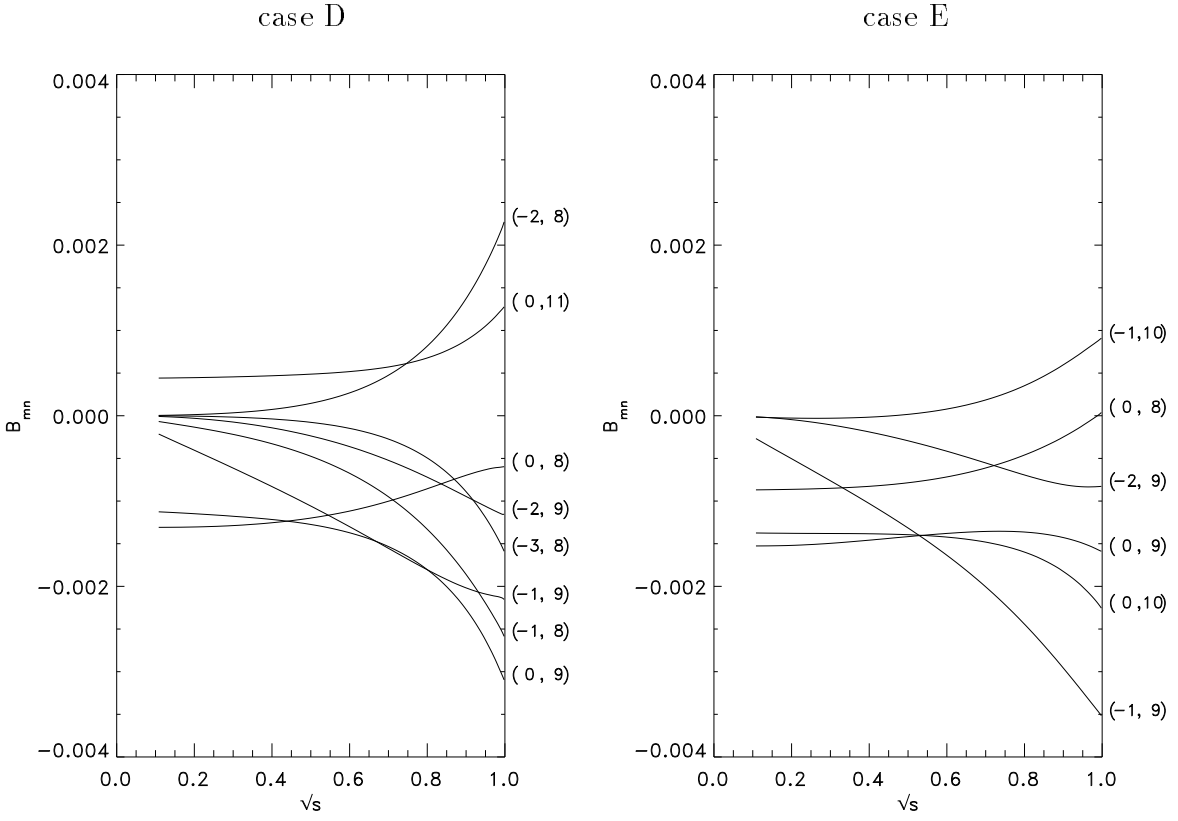

FIG. 16: Modular ripple coefficients of cases D and E versus $\sqrt{s}$ for $\langle\beta\rangle = 0.04$. Not shown, for clarity, are components with similar behaviour: $B_{-1,10}$, $B_{0,10}$, $B_{-1,11}$, $B_{2,11}$, $B_{-1,12}$, $B_{1,12}$, $B_{2,12}$ (case D) and $B_{2,11}$, $B_{1,11}$, $B_{2,10}$ (case E).

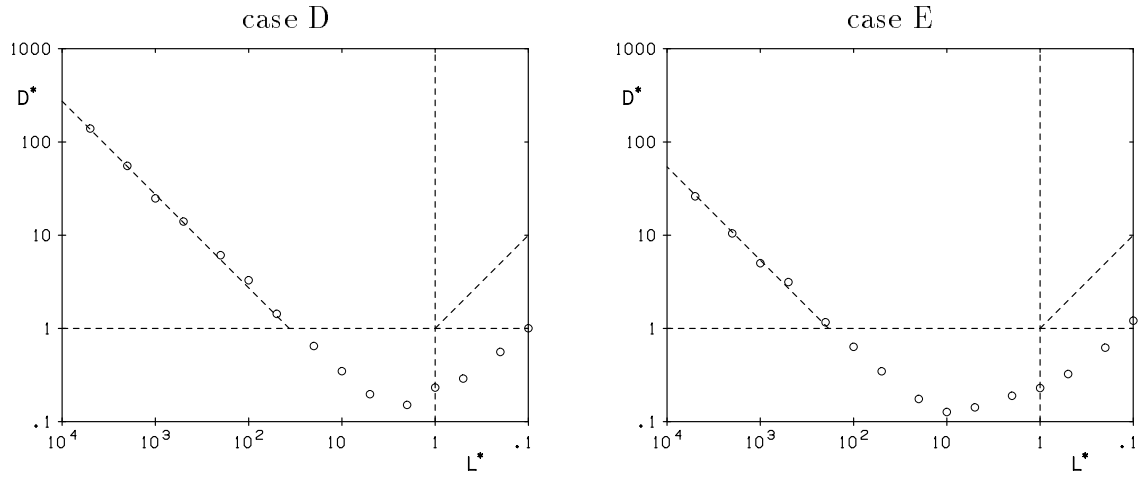

FIG. 17: Normalized transport coefficient D^* versus normalized mean free path L^* of cases D and E at approximately half the plasma radius and $\langle\beta\rangle = 0.04$. The equivalent ripple is $\delta_e = 6.5\%$ for case D and $\delta_e = 2.2\%$ for case E.

Figure 17 shows the normalized transport coefficient D^* versus the normalized mean free path L^* of cases D and E computed with Monte Carlo methods [16, 17]. The normalized mean free path is defined as $L^* = \Lambda/L_c$, where Λ is the mean free path and L_c is half the connection length. The normalized transport coefficient D^* is introduced by $D^* = D/D_p$, with D_p = plateau value. The dependence of D^* on L^* in the lmfp regime corresponds to an equivalent ripple δ_e of 6.5% for case D and 2.2% for case E. The high ripple of case D results from the large Fourier harmonic $B_{0,1}$, which determines the mirror field, in combination with the other Fourier components which are present here. A reduction of this component as done in case E, leads to a reduction of the equivalent ripple. So, only case E with an equivalent ripple of 2.2% fulfils the optimization criterion of small neoclassical transport in the lmfp regime. The other two neoclassical optimization criteria - small bootstrap current in the lmfp regime and good collisionless α-particle confinement - will, therefore, here only be investigated for case E.

5.2 Bootstrap current

Besides the classical MHD-equilibrium finite-β effect on the rotational transform, also the bootstrap current influences the rotational transform profile. It has therefore to be sufficiently small to avoid large influences on the vacuum rotational transform which may lead to critical low-order $\iota = \mathrm{n/m}$ values in the case of low shear.

In order to determine the bootstrap current of case E again a Monte Carlo simulation technique is used, that is, an ensemble of monoenergetic simulation particles is pushed in time (drift orbit tracing and pitch angle scattering). This procedure leads to an averaged parallel current, namely the bootstrap current $\langle v_{||} \rangle$ (for details see [18] and references quoted therein).

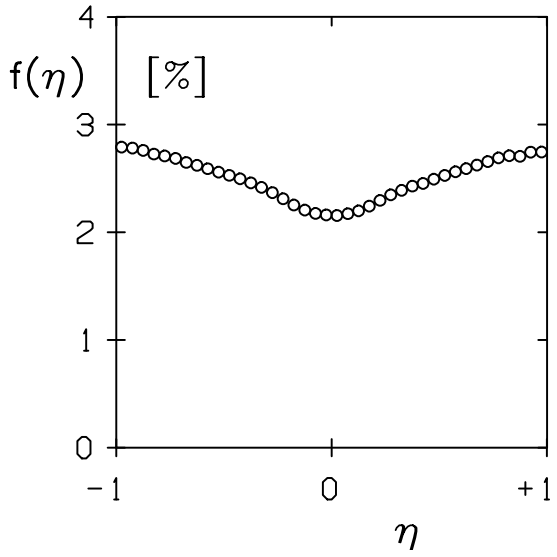

FIG. 18: Monoenergetic Monte Carlo distribution averaged over the plasma radius as a function of the pitch angle for case E $\langle\beta\rangle = 0.04$. *Dimensionless parameters for this simulation are the ratio of the plasma radius a to the gyro radius* ρ, $Q_\rho = \frac{a}{\rho} = 10^2$, *and the ratio of the mean free path* Λ *to half the connection length* $L_c = \pi R/\iota$, $L^* = \Lambda/L_c = 10^3$.

Figure 18 shows the monoenergetic Monte Carlo distribution averaged over the plasma radius as a function of the pitch angle $\eta = v_{||}/v$ for case E. The very small asymmetry of the distribution function indicates a rather small bootstrap current, $\langle\eta\rangle = -0.3\%$. The equivalent tokamak bootstrap current [19] is $\langle\eta\rangle_{\mathrm{Tok}} = -\frac{1.4\sqrt{A}}{\iota Q_\rho} = -5.2\%$, that is $\frac{\langle\eta\rangle}{\langle\eta\rangle_{\mathrm{Tok}}} = 0.06$.

5.3 Collisionless α-particle confinement

The W7-X device attempts to combine small equivalent ripple, vanishing bootstrap current and sufficiently good collisionless α-particle confinement; the latter by creating poloidally closed $\mathcal{J}$-contours at finite β, with $\mathcal{J}$ the second adiabatic invariant, $\mathcal{J} = \int v_{||} dl$.

For computing the collisionless α-particle confinement guiding centre orbits of a sample of α-particles are started at a given aspect ratio A with random values of θ, ϕ and the pitch angle $\eta = v_{||}/v$. From this sample a sample of particles which ever get reflected is obtained and the long time collisionless orbits of these are then followed (for more details see [20]).

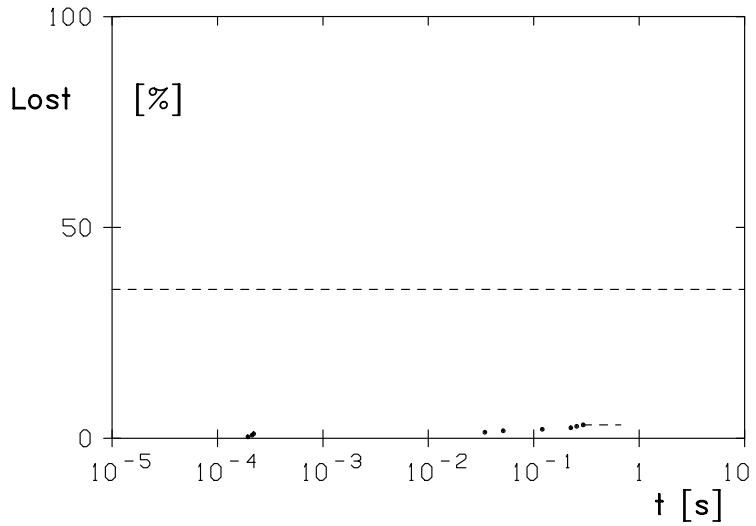

FIG. 19: α-particle losses as a function of the collisionless time of flight for case E $\langle\beta\rangle = 0.04$. 35% of the particles get reflected (dashed line) and only 5% of them get lost within the slowing-down time of $\approx 0.1s$.

Figure 19 shows the α-particle losses as a function of the collisionless time of flight. From a sample of particles (100%) 35% of the particles get reflected and only 5% of them get lost. That is, case E with $\langle\beta\rangle = 0.04$ obviously exhibits a good collisionless α-particle confinement within the slowing-down time of $\approx 0.1s$.

6. Summary and outlook

Magnetic fields and finite-β equilibria of five coil current distributions (A: standard case, B: high-ι case, C: high-ι, high-mirror case, D and E: high-ι, high-mirror, low-shear cases) produced by the coil set HS5V10T have been investigated with respect to their MHD and neoclassical properties. For this purpose, an iteration procedure based on several numerical codes has been used. As a result, case E was found to fulfil all optimization criteria. Thus, the coil set HS5V10T is suitable for the attainment of a stable, high-ι, high-mirror, low-shear, high-β plasma equilibrium.

The iteration procedure is a useful tool to compute coil current distributions which will serve as an input in order to realize experimentally specific magnetic field configurations. A survey of coil currents representing interesting configurations within the flexibility space of W7-X will be useful.

Acknowledgments

We want to thank J. Nührenberg for many useful suggestions and discussions, as well as J. Kisslinger for providing the coil currents and U. Schwenn for Figure 1.

REFERENCES

[1] GRIEGER, G., BEIDLER, C., HARMEYER, E., JUNKER, J., KISSLINGER, J., LOTZ, W., MERKEL, P., MONTVAI, A., NÜHRENBERG, J., RAU, F., SCHLÜTER, A., WOBIG, H., ZILLE, R., in Plasma Physics and Controlled Nuclear Fusion Research (Proc. 12th Int. Conf. Nice 1988) Vol. **2**, IAEA, Vienna (1989) 369.

[2] GRIEGER, G., LOTZ, W., MERKEL, P., NÜHRENBERG, J., SAPPER, J., STRUMBERGER, E., WOBIG, H., the W7-X TEAM, BURHENN, R., ERCKMANN, V., GASPARINO, U., GIANNONE, L., HARTFUSS, H.J., JAENICKE, R., KÜHNER, G., RINGLER, H., WELLER, A., WAGNER, F., the W7-AS TEAM, Phys. Fluids B **4** (1992) 2081.

[3] LOTZ, W., NÜHRENBERG, J., SCHWAB, C., Plasma Physics and Controlled Nuclear Fusion Research (Proc. 13th Int. Conf., Washington, 1990) Vol. **2**, IAEA, Vienna (1991) 603.

[4] NÜHRENBERG, J., ZILLE, R., Phys. Lett. A **114** (1986) 129.

[5] NÜHRENBERG, J., ZILLE, R., Phys. Lett. A **129** (1988) 113.

[6] MERKEL, P., Nuclear Fusion **27** (1987) 867.

[7] Wendelstein Project Group, Euratom-IPP Association, Wendelstein 7-X, Phase I, Application for Preferential Support, 1990.

[8] Wendelstein Project Group, Euratom-IPP Association, Wendelstein 7-X, Phase II, Application for Preferential Support, 1994.

[9] KISSLINGER, J., in Proc. of 6th Workshop on Wendelstein 7-X and Helias Reactors, Schloß Ringberg, Tegernsee, 20-24 Nov. 1995, IPP 2/331 (1996) 148.

[10] STRUMBERGER, E., Nuclear Fusion **36** (1996) 891.

[11] HIRSHMAN, S.P., Lee, D.K., Comput. Phys. Commun. **39** (1986) 161.

[12] HIRSHMAN, S.P., van RIJ, W.I., MERKEL, P., Comput. Phys. Comm. **43** (1986) 143.

[13] STRUMBERGER, E., Nuclear Fusion, in print.

[14] NÜHRENBERG, J., ZILLE, R., Proc. 12th EPS Conf. on Contr. Fusion and Plasma Physics, Budapest 1985, EPS, Vol **9F**, Part I, 445.

[15] NÜHRENBERG, J., ZILLE, R., in Proc. Workshop on Theory of Fusion Plasma, Varenna 1987, Eds. A. Bondesin, E. Sindoni, F. Troyon, 1988, EUR 11336 EN, 3.

[16] LOTZ, W., NÜHRENBERG, J., SCHLÜTER, A., J. Comput. Phys., **73** (1987) 73.

[17] LOTZ, W., NÜHRENBERG, J., Phys. Fluids **31** (1988) 2984.

[18] MAASSBERG, H., LOTZ, W., NÜHRENBERG, J., Phys. Fluids B **5** (1993) 3728.

[19] LOTZ, W., in Proc. of 3rd Workshop on Wendelstein 7-X, Schloß Ringberg, Tegernsee, 26-30 June 1989, IPP 2/302 (1989) 31.

[20] LOTZ, W., MERKEL, P., NÜHRENBERG, J., STRUMBERGER, E., Plasma Phys. and Contr. Fusion **34** (1992) 1037.

[21] KISSLINGER, J., BEIDLER, C.D., HARMEYER, E., RAU, F., RENNER, H., WOBIG, H., Proc. 21th EPS Conf. on Contr. Fusion and Plasma Physics, Montpellier 1994, ECA, Vol **18B**, Part I, 368.

[22] GREUNER, H., BITTER, W., KERL, F., KISSLINGER, J., RENNER, H., in Fusion Technology 1994 (Proc. of 18th Symp. on Fusion Technology, Karlsruhe 1994) Vol **1**, ELSEVIER SCIENCE B.V., Amsterdam (1995) 323.

[23] HIRSHMAN, S.P., MEIER, H.K., Phys. Fluids **28** (1985) 1387.

[24] MERKEL, P., J. Comput. Phys. **66** (1986) 83.

[25] BOOZER, A., Phys. Fluids **23** (1980) 904.

[26] MERCIER, C., in Plasma Physics and Contr. Nucl. Fusion Res. 1961, Nucl. Fusion 1962 Suppl. 2, IAEA, Vienna (1962) 801.

[27] GLASSER, A.H., GREEN, J.M., JOHNSON, J.L., Phys. Fluids **18** (1975) 875.

[28] SCHWAB, C., Theory of Fus. Plasma (Chexbres, 1988), Editrice Compositori, Bologna (1989) 85.

Appendix: numerical parameters

The codes summarized in Fig. 2 use numerous numerical parameters which are given in this appendix.

- **INPUT:**

  The coil currents of the 50 modular and 20 auxiliary coils, which are normalized to a major radius $R_0 = 5.5$ m are represented by central, infinitely thin filaments. These filaments are discretized in 96 straight filaments in case of the modular coils and 48 straight filaments in case of the auxiliary coils.

- **GOURDON CODE:**

  The vacuum magnetic field is determined on a grid. The cylindrical grid box covers the relevant region inside the first wall. It is centred around $R_0 = 5.5$ m, $Z_0 = 0$ m with a side length of $\Delta R = 2.5$ m and $\Delta Z = 2.8$ m. The box is divided into 200 toroidal grid points per period, 101 radial grid points and 101 grid points in Z-direction. This discretization corresponds to a cell size of $0.035\ \mathrm{m} \times 0.025\ \mathrm{m} \times 0.028\ \mathrm{m}$.

  For field line tracing a step size of 0.022 m has been chosen. It guarantees a high numerical accuracy. The number of toroidal transits, for which the field lines are traced, varies between at least 15 for inner closed magnetic surfaces and 250 transits for determining the position of the lcms for finite-β fields. The position of the lcms is determined with an accuracy ≤ 0.001 m at the midplane of the bean-shaped cross-section in outward direction.

  A field line which is used in the DESCUR code to approximate the lcms by a set of Fourier coefficients is traced for 75 transits and the coordinates along the field line are computed at 64 cross-sections per period.

- **DESCUR CODE:**

  The Fourier approximations of the last closed magnetic surfaces are made for m + 1 poloidal modes (m = 14) and 2n + 1 toroidal modes (n = 12). For this purpose, 300 coordinate points of the corresponding field line in poloidal direction and 64 coordinate points per period in toroidal direction are used.

- **VMEC/NEMEC CODE:**

  These codes are energy minimizing fixed/free boundary codes assuming nested flux surfaces. The cylindrical coordinates $R(s,u,v)$, $Z(s,u,v)$ and $\phi(v)$ (the cylindrical

angle $\phi(v)$ should not be confused with the magnetic coordinate ϕ) are expanded in Fourier series [11, 12]:

$$R(s,u,v) = \sum_{\mathrm{m=0,n=-n_v}}^{\mathrm{m_u,n_v}} \hat{r}(s)_{\mathrm{m,n}} \cos 2\pi(\mathrm{m}u - \mathrm{n}v),$$

$$Z(s,u,v) = \sum_{\mathrm{m=0,n=-n_v}}^{\mathrm{m_u,n_v}} \hat{z}(s)_{\mathrm{m,n}} \sin 2\pi(\mathrm{m}u - \mathrm{n}v),$$

$$\phi(v) = \frac{2\pi}{\mathrm{N_p}} v.$$

Here, s is the normalized radial flux coordinate from $s = 0$ (axis) to $s = 1$ (plasma boundary), u (poloidal) and v (toroidal) are angle-like variables ($0 \leq u, v < 1$) and $\mathrm{N_p}$ gives the number of periods ($\mathrm{N_p} = 5$). For the calculations $\mathrm{m_u} + 1$ poloidal modes ($\mathrm{m_u} = 14$) and $2\mathrm{n_v} + 1$ toroidal modes ($\mathrm{n_v} = 12$) are used. The Fourier series are computed on a mesh of $\mathrm{M_u} = 60$ (poloidal direction) times $\mathrm{N_v} = 36$ (toroidal direction) times $\mathrm{N_s} = 129$ (radial direction, number of nested flux surfaces) points, that is, $\mathrm{M_u} = 4\mathrm{m_u}$ and $\mathrm{N_v} = 3\mathrm{n_v}$.

- **MFBE CODE:**

  The magnetic fields of the finite-β equilibria are determined on the same grid as used by the GOURDON code described above (for details see [13]). The vacuum field B_v outside the plasma boundary is given by

$$\mathbf{B}_\mathrm{v}(\mathbf{r}) = \mathbf{B}_0(\mathbf{r}) + \frac{1}{4\pi}\int_{\partial R} \nabla G(\mathbf{r},\mathbf{r}')(\mathbf{B}_0' \cdot d\mathbf{f}') - \frac{1}{4\pi}\int_{\partial R} \Phi(\mathbf{r}')\nabla(\nabla' G(\mathbf{r},\mathbf{r}') \cdot d\mathbf{f}'),$$

  with $G(\mathbf{r},\mathbf{r}') = \frac{1}{|\mathbf{r}-\mathbf{r}'|}$ Green's function and $\Phi(\mathbf{r})$ potential. The positions $\mathbf{r}'$ are in the boundary ∂R, while $\mathbf{r}$ represents a position outside the plasma boundary. In order to obtain a high numerical accuracy it is necessary to adapt the number of integration points in this equation for each grid point to its distance from the plasma boundary. Since this distance may be very small for some grid points a non-equidistant integration mesh is used. To this end, the smallest distance of each individual grid point from the plasma boundary and its projection (u_0, v_0) onto the boundary is determined. Around this point (u_0, v_0) the interval of integration is set to a value which is much smaller than the distance of the grid point ($\approx 1/100$ of the distance). Further away from this point the interval of integration is increased step by step to an upper limit which corresponds to the equidistant integration mesh size used far away from the grid point, that is 50 integration points in poloidal direction and 100 integration points per period in toroidal direction. This corresponds to a integration step size of ≈ 0.07 m in both directions. For distances of grid points smaller than a very small fraction ($< 2 \cdot 10^{-4}$) of the plasma radius, the magnetic field is extrapolated from the field inside the plasma boundary.

- **JMC CODE:**

The Fourier representation of the magnetic field in magnetic coordinates is made for m + 1 poloidal modes (m = 15) and 2n + 1 toroidal modes (n = 12). From these $B_{\mathrm{m,n}}$s those which are larger than $8 \cdot 10^{-4}$ are chosen.

TABLE A1: Fourier components $B_{\mathrm{m,n}}$ of cases D and E ($\langle\beta\rangle = 0.04$) which are larger than $8 \cdot 10^{-4}$ (marked by crosses).

case D

n\m	0	1	2	3	4
12		x	x		
11	x		x		
10	x				
9	x				
8	x				
7					
6	x	x			
5		x			
4	x		x	x	
3	x	x		x	x
2	x	x	x	x	x
1	x	x	x		x
0	x	x	x	x	x
-1		x	x	x	
-2		x	x		
-3		x	x		
-4		x			
-5					
-6					
-7			x	x	
-8		x	x	x	
-9		x	x		
-10		x			
-11		x			
-12		x			

case E

n\m	0	1	2	3	4	5
12						
11		x	x			
10	x		x			
9	x					
8	x					
7						
6	x					
5	x	x				
4	x		x			x
3	x	x	x	x	x	
2	x	x	x	x	x	x
1	x	x	x	x	x	x
0	x	x	x		x	
-1		x	x	x		
-2		x	x	x		
-3		x	x			
-4		x				
-5		x				
-6			x			
-7			x			
-8						
-9		x	x			
-10		x				
-11						
-12						

- **GUIDING CENTRE CODES:**

  For computing the equivalent ripple, the bootstrap current and the collisionless α-particle confinement only $B_{\mathrm{m,n}}$s larger than $5 \cdot 10^{-3}$ are used. They are listed in Table A2. The step size for tracing the guiding centres is $\approx 1/20$ of the period length.

TABLE A2: Fourier components $B_{\mathrm{m,n}}$ of cases D and E ($\langle\beta\rangle = 0.04$) which are larger than $5 \cdot 10^{-3}$ (marked by crosses).

case D

n\m	0	1	2	3
4				
3	x	x		x
2			x	x
1	x	x		
0	x	x	x	
-1				
-2		x	x	
-3				
-4				

case E

n\m	0	1	2	3
4	x			
3	x	x		
2	x		x	x
1	x	x		
0	x	x	x	
-1		x		
-2		x		
-3				
-4				